SURFACE CRACK DEVELOPMENT IN TRANSFORMATION INDUCED FATIGUE OF SMA ACTUATORS

Dimitris C. Lagoudas, Olivier W. Bertacchini,
Aerospace Engineering Department
Texas A&M University
College Station, TX 77843-3141, USA

Etienne Patoor
Laboratoire de Physique et Mécanique des Matériaux
UMR CNRS 7554/ENSAM Metz, 4 rue Augustin Fresnel
57078 Metz, France

ABSTRACT

This paper is based on the study of a post mortem analysis of shape memory alloy (SMA) actuators undergoing thermally induced martensitic phase transformation fatigue under various stress levels. Fatigue life results were obtained for both complete and partial phase transformation cycles applied to the SMA actuators. The thermal cyclic loading was induced by forced fluid convection cooling in order to increase the cycling frequency to approximately 1Hz, resulting to corrosion assisted fatigue. The combination of corrosion and reversible phase transformation under stress led to the formation of circular cracks on the surface of the cylindrical SMA wire actuators, which eventually saturated in a periodical distribution. In order to understand the stress field contributions to the microcracking in the presence of eigenstrains, a shear lag model was developed. The model accounts for eigenstrains introduced by corrosion, plastic strain accumulation with the number of cycles and the cyclic phase transformation strain. Comparison of the model predictions with crack spacing reached at fatigue failure is carried out and the reduction of fatigue life of SMA actuators under a corrosive environment is discussed.

Introduction

SMAs have seen growing use in the mechanical, medical and aerospace industries over the last decade [1]. The thermomechanical response of NiTi SMAs subject to various mechanical and thermal loads resulting in a cyclic phase transformation has been widely investigated [2-4]. However, most of the results pertain to a limited number of cycles and mainly focus on the development and stability of two-way transformation strain and the evolution of plastic strain. Mechanical fatigue properties of SMAs have been primarily studied based on the pseudoelastic response of SMAs with some key results presented by Tobushi et al. [5] and Miyazaki et al. [6]. However, thermally induced transformation fatigue is a more recent subject, where the applied level of stress has a major influence on the development of plastic strains and therefore on a low cycle fatigue performance of SMA actuators (Bigeon and Morin [7], De Araujo et al. [8], Lagoudas et al. [9], Cuellar et al. [10]).

The applied stress during the thermally induced phase transformation favors the growth of certain martensitic variants and enforces elongation of the SMA actuator during cooling below the martensitic start temperature. Upon heating, these variants transform back into the austenitic parent phase inducing strain recovery. Such transformation conditions induce an evolution of the microstructure with the number of cycles leading to a modification of the performance of the actuator (Lagoudas et al. [9], Tamura et al. [11], Morgan and Friend [12]). Recent studies by Hornbogen and Eggeler [13, 14] focus on the role of surface quality in the fatigue life of shape memory alloys. The non-reversible plastic strain developed upon transformation cycles is permanently modifying the surface morphology and can nucleate surface cracks without assistance of inclusions or grain boundaries throughout cycled domain boundaries. Surface defects under an applied stress generate stress concentrations leading to a cyclic growth of these defects.

Due to a large reversible transformation strain under applied stress, shape memory alloys are used as high energy density actuators. However, their actuation frequency is highly limited by the heat transfer rate upon cooling [15]. Fluid convection is a way to increase the frequency but the environment may become corrosive under certain conditions [16]. In the presence of a fluid environment containing an electrolyte, the applied electrical current used to heat up the SMA actuator will induce corrosion. The corrosive environment is able to penetrate the material through the fractured passivation layer, which ceases to be a barrier for corrosion due to microcracking induced by the cyclic thermal loading. These corrosion barriers have been studied and observed in SMAs for heat treatments between 300-600°C [17, 18].

In the present work, we briefly present the experimental set up and the fatigue results of thermally induced martensitic phase transformation under various stress levels for TiNiCu SMAs. Fatigue results are obtained for both complete and partial transformation cycles. A post mortem microstructural evaluation is conducted on the failed specimens. The microstructure reveals a unique periodical crack pattern on the surface with creation of a superficial brittle layer. An analysis is made to define the parameters of this embrittlement phenomenon. A shear lag model accounting for inelastic strains is applied to characterize and identify what drives the failure of this corrosive brittle layer on the surface of SMA actuators leading to ultimate actuator failure.

Experiments and selected results

TiNiCu (Ti.40Ni.10Cu, wt.%) SMA wires of 0.6 mm (0.024 in.) diameter were used to perform the present fatigue study. The gauge length of the specimens was approximately 200 mm (8 in.). The SMA wires were annealed for 15 minutes at 550°C to allow partial recrystallization and optimization of shape memory effect and fatigue properties [9]. This study relied on isobaric (isostress) thermally induced phase transformation cycles. The experimental setup was previously utilized [19] for the purpose of testing SMA NiTi actuators with "dead" loads under thermal actuation cycles, in the presence of fluid forced convection. The SMA actuators were heated through resistive heating and were cooled through a chilled, forced fluid convection cooling. Several applied stress levels were used in the isobaric experiments performed in the range between 54 MPa and 247 MPa. The measured data were the relative displacements of the two ends of the actuators during the thermal cycles using LVTD transducers. Upon heating and cooling, each phase (austenite and martensite) reached an endpoint of transformation, where no strain recovery was observed anymore. Such thermal cycles allowed to achieve complete transformation cycles (major loops) for the different stress levels. Partial transformation cycles were then possible by applying a percentage of the maximum recoverable strain for the considered stress level. In this study, we carried out fatigue experiments for complete transformation cycles (100% of maximum recoverable strain) and for partial transformation cycles with ~50% of the maximum recoverable strain) [9]. The repeated thermal cycles were conducted until final failure of the specimens.

The transformation temperatures of the SMA wires were measured using differential scanning calorimetry (DSC) and they are reported in Table 1.

Austenitic transformation temperatures	Martensitic transformation temperatures
A_s = 54.4°C	M_s = 46.7°C
A_f = 60.6°C	M_f = 39.5°C

Table 1. Transformation temperatures for TiNiCu SMA wires from stress free DSC measurement.

Figures 1 and 2 show two typical transformation induced thermal fatigue results corresponding to 100% and 50% of the total amount of recoverable transformation strain, respectively. The applied stress level is 154 MPa. One can observe from Figure 2 a larger strain measurement for each 1000 cycle increment. These measurements were used to recalibrate the percentage of transformation strain as it changes with the number of cycles. The results in these two figures give a good indication of rapid plastic strain build up, while the recoverable strain suffers from a decrease initially before it stabilizes. An important feature is the lifespan extension when going from major to a minor transformation loop.

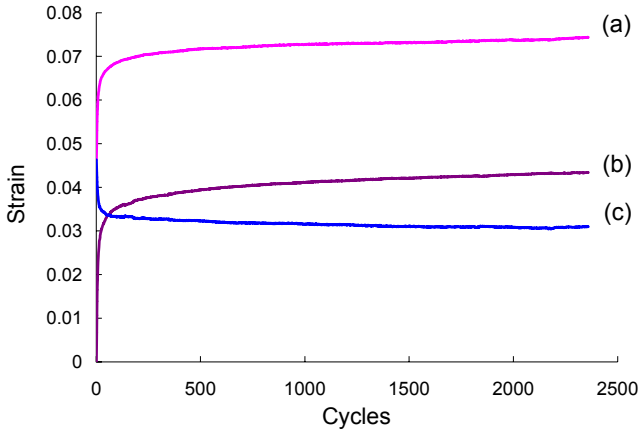

Figure 1. Complete transformation: ε-N curve for a constant applied stress of 154 MPa. The different curves show the total strain in the martensitic phase (a), austenitic phase (b) and transformation strain (c).

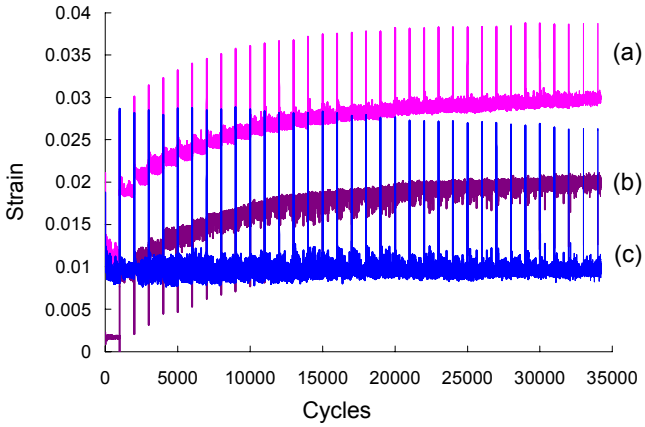

Figure 2. Partial transformation: ε-N curve for a constant applied stress of 154 MPa. The different curves show the total strain in the martensitic phase (a), austenitic phase (b) and transformation strain (c).

A summary of all fatigue results is given in Figures 3 and 4. Figure 3 reports transformation strain and plastic strain accumulation as a function of the constant applied load, while Figure 4 is a Wohler representation of the fatigue life obtained for major and minor loops experiments.

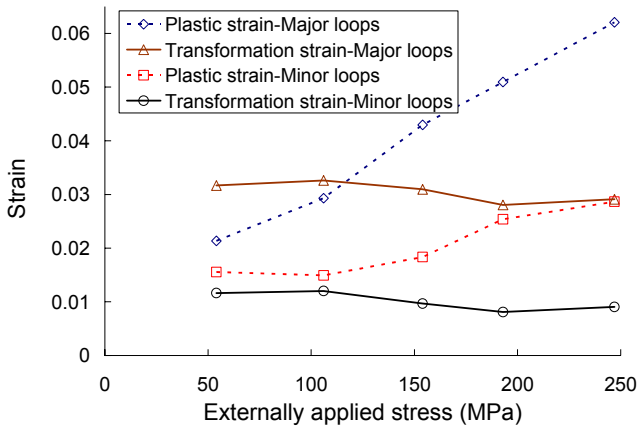

Figure 3. Evolution of plastic and transformation strains with respect to the externally applied load.

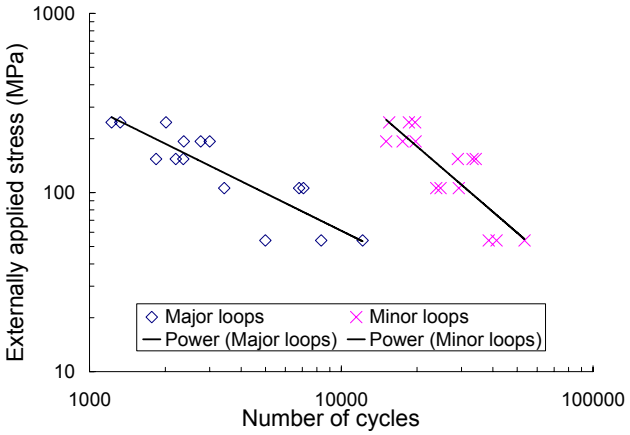

Figure 4. Wohler curve for complete and partial transformations.

Microstructural Observations

The key observation for fatigued specimens was a distribution of periodic circular cracks on both segments of broken SMA actuators. Figure 5 is an SEM micrograph of a post mortem SMA actuator exhibiting this particular microcracking structure.

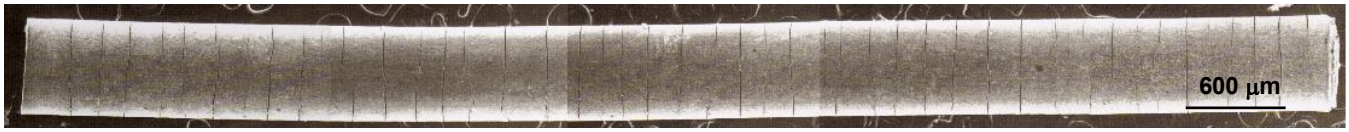

Figure 5. SEM micrograph of a SMA actuator with periodical circular cracks (total length = 8 mm, crack spacing ≈ 180 µm). The fracture surface can be seen on the right hand side of the specimen. Complete transformation cycles, applied stress 247 MPa.

It seems plausible that, under cyclic phase transformation, the protective surface oxide layer on the SMA wires is fragmented and oxide free martensitic variants are exposed to the environment, which is a mixture of water and glycol, with an electric current passing through the SMA actuator during every cycle. This corrosive environment leads to the creation of a SMA brittle layer saturated with cyclically formed and inserted oxides. This proposed surface embrittlement mechanism is supported by the observation of a thickness of embrittlement related to the lifespan of the SMA actuators. Figures 6 and 7 characterize the brittle superficial layer formed during the thermal cycles. The thickness of that layer appears to increase from ~40µm to ~70µm when the number of cycles increases from ~1200 cycles to ~15000 cycles under the same applied stress. Composition analysis of the SMA brittle layer has not been carried out yet. However, similar conditions have been identified with a preponderant formation of TiO_2 oxide [16, 17]. The superficial formation of TiO_2 generates a depletion of Ti content in the sub-layer. The result is a Ni rich region at the interface SMA/oxide layer [16, 17]. From now on and for simplicity of further modeling, we will consider cyclic formation and insertion of only TiO_2 oxide in the SMA actuators.

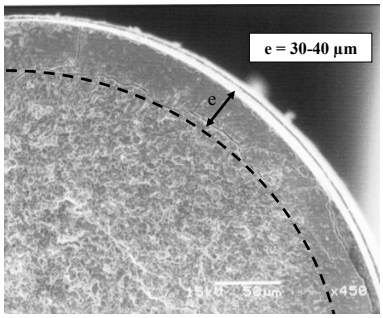

Figure 6. Micrograph of the failure surface after 1200 cycles.

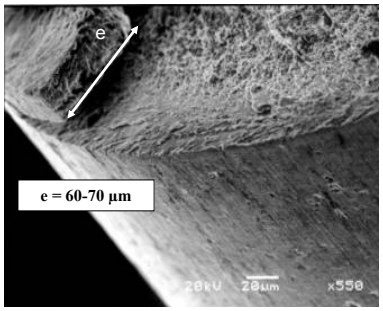

Figure 7. Micrograph of the failure surface after 15000 cycles.

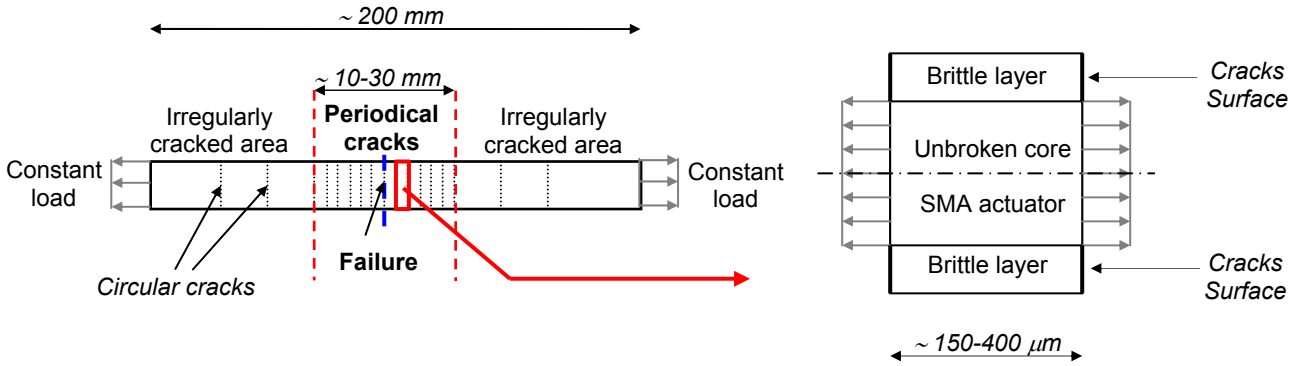

Figure 8. Schematic of the periodical microcraking pattern and identification of a representative volume element.

With the corrosion phenomenon occurring during fatigue testing, the brittle layer is continuously developing at the surface of the SMA actuators. The observation of periodical crack spacing appears to relate to a saturated distance between the circular cracks and their depth. This distance and depth vary with different parameters such as the applied stress, the amount of transformation strain, and the number of cycles. The periodicity was identified around the failure location with averaging spacing from ~100 μm to ~400 μm. The depths of the brittle layer vary from ~30 μm to ~100 μm. Figure 8 qualitatively summarizes the identification process of the periodicity with the definition of the representative volume element that will be of interest in the next section of this work. Figures 9 and 10 report the actual measurement of the depth of the brittle layer while the measured crack spacing is described in Figure 11. Figures 9 and 10 indicate the influences of both the stress level and the amount of transformation strain on the depth of the brittle layer, closely related to the fatigue life of the actuators. Figure 11 shows how two different transformation strains affect the periodical crack spacing.

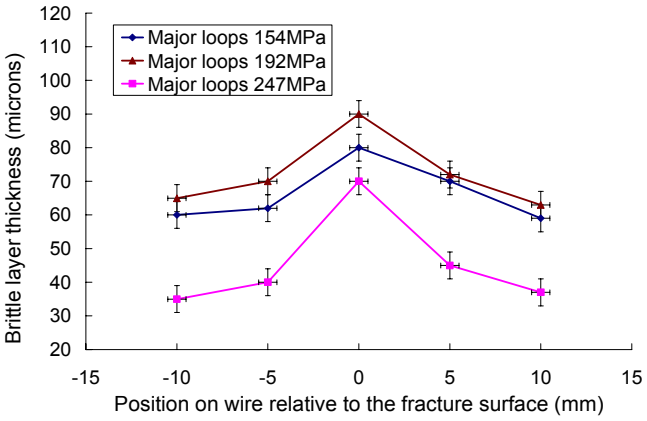

Figure 9. Brittle layer profile around failure location. Complete transformation conditions (Major loops).

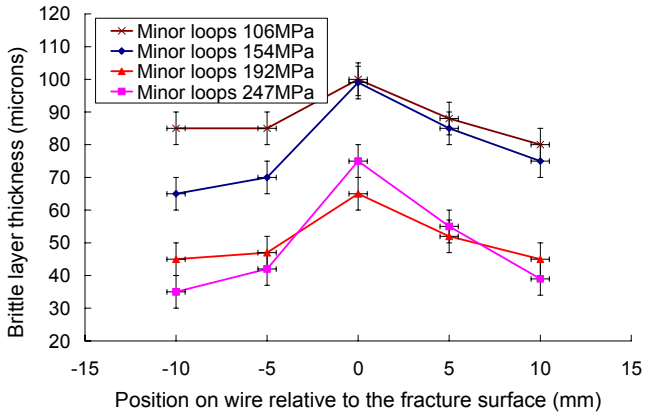

Figure 10. Brittle layer profile around failure location. Partial transformation conditions (Minor loops).

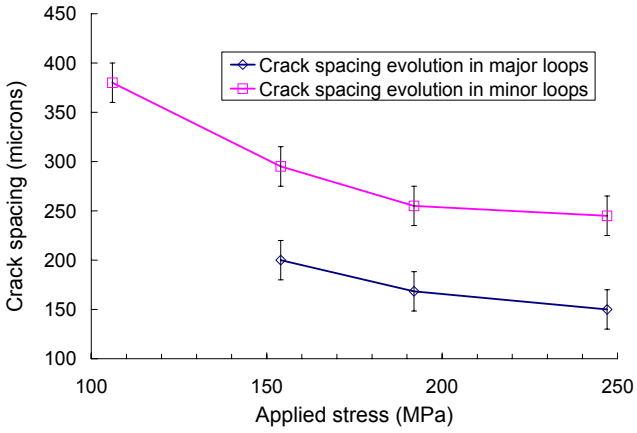

Figure 11. Crack spacing as a function of the applied stress.

Shear Lag Modeling of SMA Actuators with Circular Microcracks

The representative volume element (RVE) shown in Figure 8 is analyzed using a shear lag model in this section.

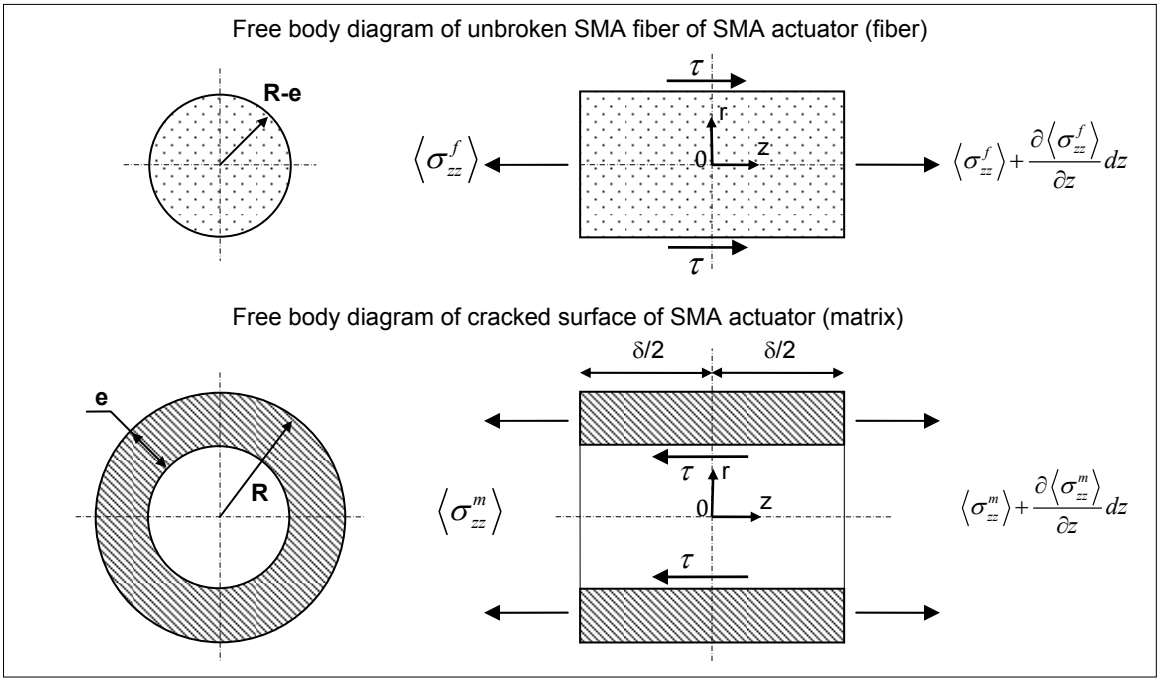

Figure 12. Free body diagrams for TiNiCu core and brittle surface layer for the shear lag model.

Force equilibrium over the respective averaged cross section areas yields:

$$\frac{\partial\langle\sigma_{zz}^f\rangle}{\partial z}+\frac{2}{R-e}\tau=0 \tag{1}$$

$$\frac{\partial\langle\sigma_{zz}^m\rangle}{\partial z}-\frac{2c_f}{(R-e)c_m}\tau=0 \tag{2}$$

Where c_f and c_m are the TiNiCu core and brittle surface layer volume fractions (the same as area fractions), respectively.

In order to reduce the number of unknowns in the above equations, one starts with the shear stress-strain constitutive relations:

$$\frac{\partial u_r^f}{\partial z}+\frac{\partial u_z^f}{\partial r}=\frac{\sigma_{rz}^f}{\mu_A^f} \text{ and } \frac{\partial u_r^m}{\partial z}+\frac{\partial u_z^m}{\partial r}=\frac{\sigma_{rz}^m}{\mu_A^m} \tag{3}$$

Where u_r^f, u_z^f, u_r^m and u_z^m are the displacements components for the fiber and matrix, respectively, and where μ_A^f and μ_A^m are the respective axial shear moduli for the fiber and matrix. Consistent with the shear lag approximation, a negligible variation of radial displacements along the fiber axis is assumed [20]:

$$\frac{\partial u_r^f}{\partial z}<<\frac{\partial u_z^f}{\partial r} \text{ and } \frac{\partial u_r^m}{\partial z}<<\frac{\partial u_z^m}{\partial r} \tag{4}$$

This reduces equations (3) to the following form:

$$\frac{\partial u_z^f}{\partial r}=\frac{\sigma_{rz}^f}{\mu_A^f} \text{ and } \frac{\partial u_z^m}{\partial r}=\frac{\sigma_{rz}^m}{\mu_A^m} \tag{5}$$

The shear stress distribution is now assumed to be of the form [21]:

$$\sigma_{rz}^{f} = \tau(z)\frac{r}{R-e} \text{ and } \sigma_{rz}^{m} = \left\{\frac{R-e}{r} - c_f \frac{r}{R-e}\right\}\frac{\tau(z)}{c_m} \tag{6}$$

Following the work of McCartney [22], one can easily define the interfacial shear stress at $r = R - e$ as proportional to the difference between the average axial displacements of the matrix and the fiber, i.e.:

$$\tau(z) = \Gamma\left(\left\langle u_z^m \right\rangle(z) - \left\langle u_z^f \right\rangle(z)\right) \tag{7}$$

With the constant Γ given by:

$$\Gamma = \frac{c_m}{(R-e)\left\{\frac{c_m}{4\mu_A^f} + \frac{1}{2\mu_A^m}\left(\frac{1}{c_m}\ln\frac{1}{c_f} - 1 - \frac{c_m}{2}\right)\right\}} \tag{8}$$

Assuming different eigenstrains for the TiNiCu core, due to phase transformation and plastic strain accumulation, and the brittle layer due to the formation of oxide, denoted by ε_{in}^{f} and ε_{in}^{m}, respectively, the constitutive equations for the axial strains are given by:

$$\varepsilon_{zz}^{f} = -\frac{\nu_A^f}{E_A^f}\left(\sigma_{rr}^{f} + \sigma_{\theta\theta}^{f}\right) + \frac{\sigma_{zz}^{f}}{E_A^f} + \varepsilon_{in}^{f} \text{ and } \varepsilon_{zz}^{m} = -\frac{\nu_A^m}{E_A^m}\left(\sigma_{rr}^{m} + \sigma_{\theta\theta}^{m}\right) + \frac{\sigma_{zz}^{m}}{E_A^m} + \varepsilon_{in}^{m} \tag{9}$$

Where E_A^f and E_A^m are axial Young's moduli, and ν_A^f and ν_A^m are axial Poisson's ratios for the core and surface layer, respectively. Averaging equations (9a) and (9b) over the cross section yields:

$$\left\langle \varepsilon_{zz}^{f} \right\rangle = \frac{\left\langle \sigma_{zz}^{f} \right\rangle}{E_A^f} + \varepsilon_{in}^{f} \text{ and } \left\langle \varepsilon_{zz}^{m} \right\rangle = \frac{\left\langle \sigma_{zz}^{m} \right\rangle}{E_A^m} + \varepsilon_{in}^{m} \tag{10}$$

We also have the following kinematic relations for infinitesimal strains:

$$\varepsilon_{zz}^{f} = \frac{\partial u_z^f}{\partial z} \text{ and } \varepsilon_{zz}^{m} = \frac{\partial u_z^m}{\partial z} \tag{11}$$

Averaging equations (11a) and (11b) and combining them with equations (1), (2), (7), (8) and (10), we can show that the interfacial shear stress $\tau(z)$ satisfies the following second order ordinary differential equation:

$$\frac{d^2\tau(z)}{dz^2} = k^2\tau(z) \tag{12}$$

Where:

$$k^2 = \frac{2E_A^*}{(R-e)^2\eta E_A^f E_A^m},\ E_A^* = c_f E_A^f + c_m E_A^m \text{ and } \eta = \frac{c_m}{4\mu_A^f} + \frac{1}{2\mu_A^m}\left(\frac{1}{c_m}\ln\frac{1}{c_f} - 1 - \frac{c_m}{2}\right) \tag{13}$$

Upon integration of equation (12) and use of equations (1) and (2), the average stresses in the core and surface layer are of the form:

$$\left\langle \sigma_{zz}^{f} \right\rangle(z) = -\frac{2}{k(R-e)}\left(-Ae^{-kz} + Be^{kz}\right) + D_f \tag{14}$$

$$\left\langle \sigma_{zz}^{m} \right\rangle (z) = \frac{2}{k\left(R-e\right)} \frac{c_f}{c_m} \left(-Ae^{-kz} + Be^{kz} \right) + D_m \tag{15}$$

Integration of the above equations leads to the following expression for the average displacements:

$$\left\langle u_{zz}^{f} \right\rangle (z) = -\frac{2}{k^2\left(R-e\right)E_A^f} \left(Ae^{-kz} + Be^{kz} \right) + \frac{D_f}{E_A^f} z + F_f \tag{16}$$

$$\left\langle u_{zz}^{m} \right\rangle (z) = \frac{2}{k^2\left(R-e\right)E_A^m} \frac{c_f}{c_m} \left(Ae^{-kz} + Be^{kz} \right) + \frac{D_m}{E_A^m} z + F_m \tag{17}$$

Where A, B, D_f, D_m, F_f and F_m are constants to be determined from the boundary conditions. The boundary conditions are defined by the externally applied load conditions, by the validity of equation (7) at $z = \frac{\delta}{2}$ and by the perfect bonding assumption at the interface, as well as symmetry requirements for the RVE. They are given below:

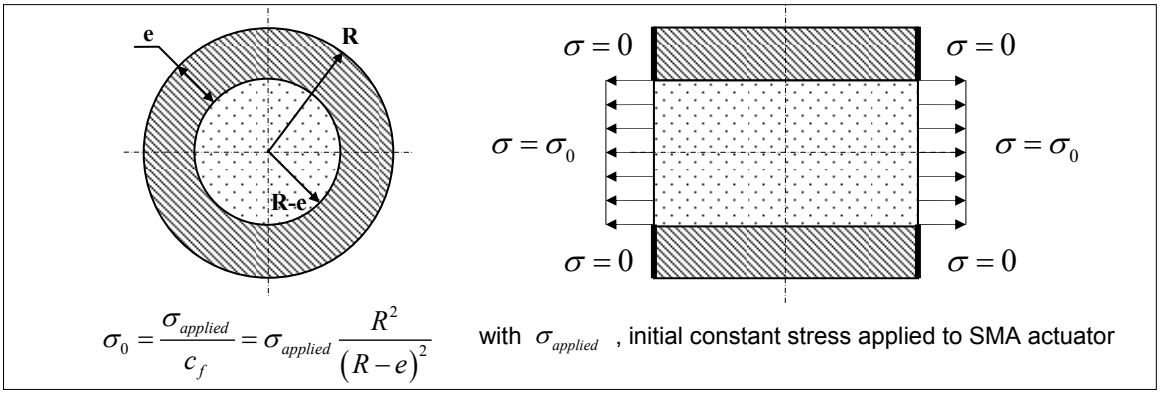

Figure 13. Schematic describing the boundary conditions for the selected RVE.

- $z = \pm\frac{\delta}{2}$

$$\left\langle \sigma_{zz}^{m} \right\rangle (z) - E_A^m \varepsilon_{in}^m = 0 \tag{18}$$

$$\left\langle \sigma_{zz}^{f} \right\rangle (z) - E_A^f \varepsilon_{in}^f = \sigma_0 \tag{19}$$

$$\tau(z) = \Gamma\left(\left\langle u_{zz}^{m} \right\rangle (z) - \left\langle u_{zz}^{f} \right\rangle (z) \right) \tag{20}$$

- $z = 0$

$$\tau(z) = 0 \tag{21}$$

$$\left\langle u_{zz}^{f} \right\rangle (z) = 0 \tag{22}$$

$$\left\langle u_{zz}^{m} \right\rangle (z) = 0 \tag{23}$$

The material parameters for the model are given in Table 2.

	TiNiCu core	Surface layer
Austenite axial Young's modulus (GPa)	67.9	69.5
Martensite axial Young's modulus (GPa)	16	18.1
Austenite axial shear modulus (GPa)	26	26.7
Martensite axial shear modulus (GPa)	6.2	7.0
Poisson's ratio	0.3	0.29

Table 2. Material parameters for TiNiCu core and surface layer.

The shear lag modeling results are shown in Figures 14 and 15 for SMA actuators initially loaded under 154 MPa. The periodical cracks induce a high stress concentration at the boundary of each unit cell. The concentration factors are 1.63 and 1.86 in complete and partial transformation, respectively, as it can be seen in the figures for $z = \frac{\delta}{2}$.

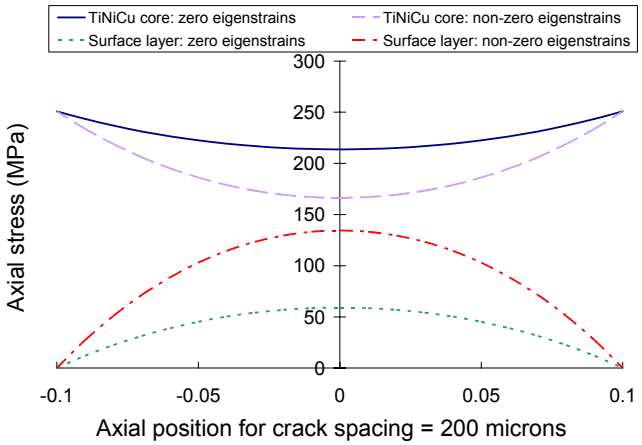

Figure 14. Axial stress profile between two circular microcracks for crack spacing: δ = 200 μm in complete transformation (total eigenstrain in the TiNiCu core 7%), external load = 154 MPa, thickness of cracked brittle layer = 65 μm, eigenstrain in surface layer = 5%.

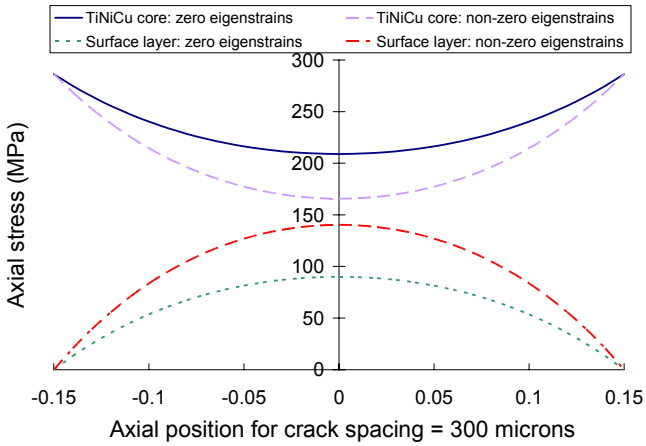

Figure 15. Axial stress profile between two circular microcracks for crack spacing: δ = 300 μm in partial transformation (total eigenstrain in the TiNiCu core of 4%), external load = 154 MPa, thickness of cracked brittle layer = 80 μm, eigenstrain in surface layer = 3%.

Eigenstrains for the unbroken SMA core are determined from the fatigue data previously obtained (transformation strain plus accumulated plastic strain). The embrittlement of the surface layer is most likely to reduce the contribution from the recoverable strain and therefore reduce the amount of accumulated plastic strain. Based on the proposed embrittlement mechanism, the amount of transformation strain is driving the level of crack spacing saturation of the surface layer with cyclic oxide insertion. This means that the higher the amount of transformation strain is, the faster saturation is reached and the higher the difference between TiNiCu core and surface layer eigenstrains is. Therefore, a parametric study is conducted to determine the amount of eigenstrain in the brittle layer. Eigenstrain values of 5% and 3% are obtained for complete and partial transformation cycles, respectively, and eigenstrain mismatches of 2% and 1% between the brittle layer and the core are identified. The shear lag results are computed in the martensitic phase, where the eigenstrains are maximum and yield a threshold value for the stress level inducing crack in the brittle layer. In both complete transformation (major loops) and partial transformation (minor loops), an almost identical stress level is attained as indicated in Figures 14 and 15, which most likely leads to the ultimate fracture of the brittle surface layer. The increase in the axial stress from the purely elastic solution (zero eigenstrains in both SMA core and surface layer), which is included for comparison purpose, indicates the influence of inelastic strains on the axial stress development in the brittle surface layer. One can also see from Figures 14 and 15 how the inelastic strains influence the stress reduction in the TiNiCu core for both complete and partial transformation cycles.

Conclusion

In this paper, a study on the thermomechanical transformation induced fatigue of SMAs under various stress levels was conducted. Complete and partial phase transformation cycles were applied. Corrosion assisted fatigue was identified using microstructural evaluation of post mortem SMA actuators. The microstructure revealed a periodical distribution of circular cracks on the cylindrical surface of the actuators. The crack distribution was related to the creation of a SMA brittle layer saturated with cyclically formed and inserted oxides. A surface embrittlement mechanism was proposed and supported by the observation of a brittle layer related to the lifespan of SMA actuators. The crack spacing was related to the amount of transformation strain applied to the SMA actuators. A shear lag model accounting for inelastic strains was derived to evaluate the stress field leading to the formation of the observed circular cracks developed in the SMA brittle layer. The amount of transformation strain, and therefore of eigenstrain mismatch, was related to the crack spacing. Occurring faster in the case of complete phase transformation cycles, the saturation of the surface layer was recognized to accelerate the damage process of the TiNiCu actuators leading to premature failure. In the case of partial phase transformation cycles, saturation was slower, leading to a thicker brittle layer with larger crack spacing. The combination of the saturation of the surface layer with the stress concentration occurring at each crack location, where the active cross section is reduced, was most likely responsible for accelerating the ultimate failure of SMA actuators and therefore reducing their fatigue life.

Acknowledgments

The authors would like to acknowledge the support of the Texas Institute for Intelligent Bio-Nano Materials and Structures for Aerospace Vehicles (TiiMS) and of the Region Lorraine from France. This effort is the result of a joint research program between the Aerospace Engineering Department at Texas A&M University and the Laboratoire de Physique et Mécanique des Matériaux (LPMM) at the Ecole Nationale Supérieure d'Arts et Métiers (ENSAM).

References

1. Birman, V., "Review of Mechanics of Shape Memory Alloy Structures", Applied Mechanics Reviews, Vol. 50 (11), 629-645, (1997).

2. Hebda, D. and White, S. R., "Effect of Training Conditions and Extended Thermal Cycling on Nitinol Two-way Shape Memory Behavior", Smart Materials and Structures Vol. 4, 298-304, (1995).

3. Bo, Z. and Lagoudas, D. C., "Thermomechanical Modeling of Polycrystalline SMAs under Cyclic Loading, Part III: Evolution of Plastic Strains and Two-Way Memory Effect", Int. J. Eng. Sci., 1175-1203, (1999).

4. Lim, T. J. and McDowell, D. L., "Degradation of a Ni-Ti alloy During Cyclic Loading", Proceedings of the North American Conference on Smart Structures and Materials, SPIE, Orlando, Florida, 153-165, (1994).

5. Tobushi, H., Hachisuka, T., Hashimoto, T., Yamada, S., "Cyclic deformation and fatigue of a TiNi shape-memory alloy wire subjected to rotating bending", Journal of Engineering Materials and Technology 120, 64-70, (1998).

6. Miyazaki, S., Mizukoshi, K., Ueki, T., Sakuma, T., Liu, Y., "Fatigue life of Ti–50 at.% Ni and Ti–40Ni–10Cu (at.%) shape memory alloy wires", Material Science and Engineering A 273-275, 658-663, (1999).

7. Bigeon, M. and Morin, M., "Thermomechanical study of the stress assisted two way memory effect fatigue in TiNi and CuZnAl wires", Scripta Materialia Vol.35 (N°12), 1373-1378, (1996).

8. C.J. De Araujo, M. Morin, G. Guénin, "Electro-thermomechanical behaviour of a Ti-45.0Ni-5.0Cu (at.%) alloy during shape memory cycling", Material Science and Engineering., A 273-275, 305-309, (1999).

9. Lagoudas, D. C., Li, C., Miller, D. A., Rong, L., "Thermomechanical transformation fatigue of SMA actuators", Proceedings of SPIE, Vol. 3992, 420-429, (2000).

10. López Cuéllar, E., Guénin, Morin, G. M., "Study of the stress-assisted two-way memory effect of a Ti–Ni–Cu alloy using resistivity and thermoelectric power techniques", Materials Science and Engineering A, Volume 358, Issues 1-2, 350-355, (2003).

11. Tamura, H., Mitose, K., Suzuki, Y., "Fatigue Properties of Ti-Ni Shape Memory Alloy Springs", J. Phys. IV, Vol. 5, C8, 617, (1995).

12. Morgan, N.B., Friend, C.M., "A review of shape memory stability in NiTi alloys", J. Phys. IV, C11, 325-332, (2001).

13. Hornbogen, E. and Eggeler, G., "Surface Aspects in Fatigue of Shape Memory Alloys (SMA)", Materialwissenschaft und Werkstofftechnik, Volume 35, Issue 5 , 255-259, (2004).

14. Hornbogen, E., "Review Thermo-mechanical fatigue of shape memory alloys", Journal of Material Science, Vol. 39, 385-399, (2004).

15. Miller, D. A., "Thermomechanical characterization of plastic deformation and transformation fatigue in Shape Memory alloys", PhD thesis, Texas A&M University, (2000).

16. Shabalovskaya S. A., "Surface, corrosion and biocompatibility aspects of Nitinol as an implant material", Bio-Medical Materials and Engineering, Vol. 12, 69–109, (2002).

17. Firstov, G.S., Vitchev, R.G., Kumar, H., Blanpain, B., Van Humbeeck, J., "Surface oxidation of NiTi shape memory alloy", Biomaterials, Vol. 23, 4863-4871, (2002).

18. Ishida, A. and Sato, M., "Thickness effect on shape memory behavior of Ti-50.0at.%Ni thin film", Acta Mat., Vol. 51, 5571-5578, (2003).

19. Bertacchini, O., Lagoudas, D., Patoor, E., “Fatigue life characterization of shape memory alloys undergoing thermomechanical cyclic loading”, Proceedings of SPIE, Vol. 5053, 612-624, (2003).

20. Nairn, J.A., “On the use of shear-lag methods for analysis of stress transfer in unidirectional composites”, Mechanics of Materials, vol. 26, 63-80, (1997).

21. McCartney, L. N., “New Theoretical Model of Stress Transfer between Fibre and Matrix in a Uniaxially Fibre-Reinforced Composite”, Proc. R. Soc. Lond., vol. A425, 215-244, (1989).

22. McCartney, L. N., “Analytical Models of Stress Transfer in Unidirectional Composites and Cross-Ply Laminates, and Their Application to the Prediction of Matrix/Transverse Cracking”, Local Mechanics Concepts for Composite Material Systems, Proc. IUTAM Symposium, Blacksburg, VA, 251-258, (1991).